PNAS RESEARCH ARTICLE | BIOPHYSICS AND COMPUTATIONAL BIOLOGY
PLANT BIOLOGY

On the mechanical origins of waving, coiling and skewing in *Arabidopsis thaliana* roots

Amir Porat[a,b], Arman Tekinalp[c], Yashraj Bhosale[c], Mattia Gazzola[c,1], and Yasmine Meroz[b,d,1]

Edited by Daniel Goldman, Georgia Institute of Technology, Atlanta, GA; received July 25, 2023; accepted December 7, 2023 by Editorial Board Member Dominique C. Bergmann

By masterfully balancing directed growth and passive mechanics, plant roots are remarkably capable of navigating complex heterogeneous environments to find resources. Here, we present a theoretical and numerical framework which allows us to interrogate and simulate the mechanical impact of solid interfaces on the growth pattern of plant organs. We focus on the well-known waving, coiling, and skewing patterns exhibited by roots of *Arabidopsis thaliana* when grown on inclined surfaces, serving as a minimal model of the intricate interplay with solid substrates. By modeling growing slender organs as Cosserat rods that mechanically interact with the environment, our simulations verify hypotheses of waving and coiling arising from the combination of active gravitropism and passive root-plane responses. Skewing is instead related to intrinsic twist due to cell file rotation. Numerical investigations are outfitted with an analytical framework that consistently relates transitions between straight, waving, coiling, and skewing patterns with substrate tilt angle. Simulations are found to corroborate theory and recapitulate a host of reported experimental observations, thus providing a systematic approach for studying in silico plant organs behavior in relation to their environment.

plants | tropism | morpho-elasticity | pattern formation | mechanics

Significance

Plant roots exhibit an exceptional ability to navigate in heterogeneous soil environments while overcoming obstacles. Our study combines theory and experimental observations to interrogate and simulate the mechanical impact of obstacles on organ growth. As a test case, we focus on well-known observations of waving, coiling, and skewing growth patterns of *Arabidopsis thaliana* roots grown on inclined substrates. Overall, our study explains a broad set of experimental observations through the minimal ingredients of gravitropism and passive mechanics. Our numerical framework provides an in silico laboratory, yielding quantitative insight into the dynamics of growing organs at the intersection of active processes and passive mechanics, applicable beyond plants to any slender growing system, from neurons or fungal hyphae to novel soft robots.

The ability of roots to grow in soil is critical for plant health and crop yield, enabling the uptake of water and nutrients, providing anchorage and stability of eroding soil (1–4). This is no small feat. Indeed, soil is a highly heterogeneous environment, characterized by nonuniform concentrations of resources as well as obstacles such as rocks and compacted soil. In negotiating with the environment, plant roots combine passive physics and active growth-driven mechanisms, termed tropisms, whereby dedicated organs sense stimuli such as water (hydrotropism) or gravity (gravitropism), and redirect growth appropriately. While dynamics of tropisms are generally understood (5, 6), and aspects of root mechanics and their effect on growth have been described (7–11), a consistent framework to dissect the interplay between passive and active responses, heterogeneous environments and ensuing growth patterns, is still missing (12–14). The essence of this complex interaction is on display in controlled experiments of roots growing on inclined agar gel substrates, whereby remarkably different behaviors are observed to emerge: roots grow straight on vertical planes, grow in waving patterns as tilt increases, skew in some cases, and eventually coil when tilt approaches the horizontal plane (Fig. 1*A*). These growth patterns are well-documented in genetically driven phenotypes of *Arabidopsis thaliana* (15–21). Although insightful, such genetic approaches are limited to given species, and do not formally address the fundamental role of root and environmental mechanics. Thus, while gravitropic responses and root-substrate mechanics clearly play a role (17, 22), underlying mechanisms remain subject of debate. For instance, both circumnutation (16, 23–25), the intrinsic circular movements of root tips, and thigmotropism (15, 22, 26), the active response to touch, have been suggested to be at the basis of waving and skewing patterns. Here, we combine advances in the modeling of growing rod-like organs (25, 27–36) and 3D numerical simulations (37) to gain broader insight.

Results

Modeling of Root Mechanics and Growth. In modeling the waving and coiling experiments of *Arabidopsis thaliana*, we begin by assuming separation of timescales between slow growth-driven root responses and fast mechanical relaxation (Fig. 1*D*), allowing us to decouple the two processes in a quasi-static manner (28, 29).

Slender roots are represented as Cosserat rods (37), which are 1D elastic continuous elements able to undergo all modes of deformations—bending, twisting, stretching,

Author contributions: A.P., A.T., Y.B., M.G., and Y.M. designed research; performed research; analyzed data; and wrote the paper.

The authors declare no competing interest.

This article is a PNAS Direct Submission. D.G. is a guest editor invited by the Editorial Board.

[1]To whom correspondence may be addressed. Email: mgazzola@illinois.edu or jazz@tauex.tau.ac.il.

This article contains supporting information online at https://www.pnas.org/lookup/suppl/doi:10.1073/pnas.2312761121/-/DCSupplemental.

Published March 6, 2024.

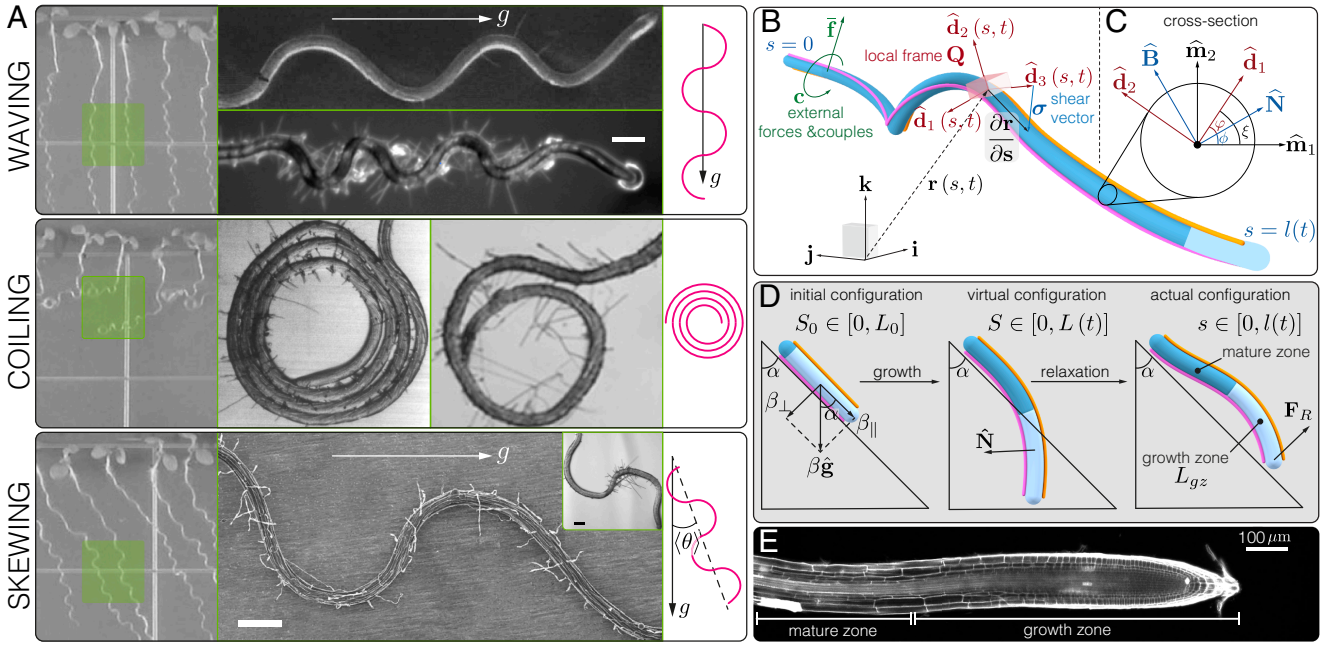

Fig. 1. (*A*) Growth patterns of Arabidopsis thaliana roots grown on inclined agar plates. *Arabidopsis thaliana* roots are grown on inclined agar plates. While roots grow straight when the plane is vertical, at low inclinations roots tend to grow in waving patterns (17, 19, 23), and at some critical angle they coil (16, 19, 20). A number of mutants also skew at an angle $\langle\theta\rangle$ (19, 38, 39). On the *Left*, the growth patterns are shown on the scale of the whole plant (19). Green squares highlight the morphologies of interest, magnified in the *Middle* panels, and schematically illustrated on the *Right*. Model definitions. (*B*) Cosserat rod. Shape is defined in space with $\boldsymbol{r}(s,t)$ along the center-line s at time t, and a local orthonormal material frame $\{\mathbf{d}_1(s,t), \mathbf{d}_2(s,t), \mathbf{d}_3(s,t)\}$ (orange and pink lines mark $\pm\mathbf{d}_1(s,t)$). Densities of external forces $\boldsymbol{f}(s,t)$ and couples $\boldsymbol{c}(s,t)$ cause the rod to deform elastically. The curvature vector $\boldsymbol{\kappa}(s,t)$ describes how the material frame bends and twists along the center-line, and the local vector $\boldsymbol{\sigma}(s,t)$ describes how the rod shears and stretches. The light blue region near the tip represents the growth zone. (*C*) Cross-section plane. $\mathbf{d}_1$ and $\mathbf{d}_2$ are the material frame directors, and $\mathbf{d}_3$ points to the reader. $\hat{\mathbf{m}}_1$ and $\hat{\mathbf{m}}_2$ represent an arbitrary normal development of the center-line, or the Bishop frame (40). $\hat{\mathbf{N}}$ and $\hat{\mathbf{B}}$ are the normal and bi-normal directors of the Frenet-Serret frame. The angle ϕ between $\hat{\mathbf{m}}_1$ and $\hat{\mathbf{N}}$ is related to the torsion of the center-line (*SI Appendix*, 2). Twist is described by the arc-length variations in the angle $\xi = \phi + \varphi$, between $\hat{\mathbf{m}}_1$ and $\mathbf{d}_1$. (*D*) Integration scheme. (*Left*) Initial geometry of our simulations, where a root of length L_0 is placed on a surface inclined at an angle α from the vertical, parameterized by an initial arc-length $S_0 \in [0, L_0]$. The differential growth vector related to gravitropism is parallel to the direction of gravity (see main text), and can be decomposed into normal and parallel components with respect to the plane (*SI Appendix*, 6). The *Center* and *Right* panels describe the two-step numerical integration scheme detailed in the *Methods*. (*Center*) Growth-driven changes implemented to the reference configuration, following Eqs. **3** and **4**, lead to an intermediate virtual configuration disregarding elastic responses. The arc-length is parameterized by $S \in [0, L(t)]$, related to the initial configuration through the growth stretch $\lambda_g(S_0,t) = \partial S/\partial S_0$. (*Right*) Relaxation to mechanical equilibrium following Eqs. **1** and **2**. The actual configuration of the rod is parameterized by $s \in [0, l(t)]$, related to the virtual configuration through the elastic stretch $\lambda_e(S,t) = \partial s/\partial S$. (*E*) Roots axial growth profile. Micrograph of an *Arabidopsis thaliana* root. Cells divide at the tip, and elongate within the growth zone, until they stop elongating, reaching the mature zone. Image courtesy of Eilon Shani.

shearing—and reconfigure in 3D space (Fig. 1*B*). We mathematically describe a slender rod by a centerline $\mathbf{r}(s,t) \in \mathbb{R}^3$ and a rotation matrix $\mathbf{Q}(s,t) = \{\mathbf{d}_1, \mathbf{d}_2, \mathbf{d}_3\}^{-1}$, providing a local material frame. When the rod is at rest, its length is L and the corresponding material coordinate is $S \in [0, L]$, while l and $s \in [0, l]$ denote the length and arc-length of the deformed (stretched) filament, and t is time. If the rod is unsheared, $\mathbf{d}_3$ points along the centerline tangent $\frac{\partial \mathbf{r}}{\partial s}$, while $\mathbf{d}_1$ and $\mathbf{d}_2$ span the normal–binormal plane, i.e., the cross-section. Shearing and stretching shift $\mathbf{d}_3$ away from $\frac{\partial \mathbf{r}}{\partial s}$, quantified by the shear vector $\boldsymbol{\sigma} = \left(\lambda_e \frac{\partial \boldsymbol{r}}{\partial s} - \mathbf{d}_3\right)$, where $\lambda_e \equiv \partial s/\partial S$ is the local elastic stretch. The curvature vector $\boldsymbol{\kappa} = \kappa_1\mathbf{d}_1 + \kappa_2\mathbf{d}_2 + \kappa_3\mathbf{d}_3$ encodes the rotation rate of the local frame along the material coordinate so that $\frac{\partial}{\partial s}\mathbf{d}_j = \boldsymbol{\kappa} \times \mathbf{d}_j$. We define the bending stiffness matrix $\mathbf{B}$ and shearing stiffness matrix $\mathbf{S}$ in the rest configuration. Then, the mechanical equilibrium of a rod-like root is described by

$$\frac{\partial \boldsymbol{n}}{\partial s} + \boldsymbol{f} = 0, \qquad [1]$$

$$\frac{\partial \boldsymbol{m}}{\partial s} + \frac{\partial \boldsymbol{r}}{\partial s} \times \boldsymbol{n} + \boldsymbol{c} = 0, \qquad [2]$$

where $\boldsymbol{n} = \mathbf{S}(\boldsymbol{\sigma} - \boldsymbol{\sigma}^0)$ represents internal forces, related to shear and elastic stretch of the centerline, $\boldsymbol{m} = \mathbf{B}\left(\boldsymbol{\kappa} - \boldsymbol{\kappa}^0\right)$ represents internal torques, related to bending and twisting, and $\boldsymbol{\sigma}^0$ and $\boldsymbol{\kappa}^0$ are intrinsic strains. As detailed in ref. 37, incompressibility is incorporated by rescaling $\mathbf{B}$, $\mathbf{S}$ and $\boldsymbol{\kappa}$ through λ_e such that $\mathbf{B} \to \mathbf{B}/\lambda_e^2$, $\mathbf{S} \to \mathbf{S}/\lambda_e$ and $\boldsymbol{\kappa} \to \boldsymbol{\kappa}/\lambda_e$. Last, external forces $\boldsymbol{f}$ and torques $\boldsymbol{c}$ (per unit length) capture overall environmental effects.

Next, we outfit this model with active gravitropic dynamics driven by differential growth (30, 41, 42). Axial growth is implemented via the additional stretch factor λ_g, defined with respect to an initial material coordinate $S_0 \in [0, L_0]$, such that L_0 is the initial length and $\lambda_g \equiv \partial S/\partial S_0$ (Fig. 1*D*). By denoting time derivatives as $\frac{dx}{dt} = \dot{x}$, we introduce the average relative growth rate as $\dot{\varepsilon}_g \equiv \dot{\lambda}_g/\lambda_g$. Root growth is restricted to a finite growth zone of length L_{gz} extending from the tip (Fig. 1*E*), reflecting experimental evidence (8, 43, 44).

Tropic movements are directed by environmental cues, which are generally perceived via dedicated sensory systems. Gravity in particular is sensed via specialized cells close to the tip (45), and translated into a redistribution of growth hormones across the root cross-section. This results in axial differential growth, which in turn leads to a change in the root's curvature, redirecting the organ toward the stimulus. This machinery is mathematically captured via the local differential growth vector $\boldsymbol{\Delta}(s,t)$ (30, 41, 42)

$$\boldsymbol{\Delta}(s,t) = \beta\hat{\boldsymbol{g}} - \gamma R\kappa(s,t)\hat{\mathbf{N}}(s,t), \qquad [3]$$

where the first term represents the gravity stimulus, with $\hat{\boldsymbol{g}}$ the direction of gravity and β the gravitropic gain or sensitivity (41). The second term represents the proprioceptive response. This can be thought of as a counter-curving response that balances the gravitropic one, based on the sensing of the organ's own shape (41). Here γ is the proprioceptive gain, $\kappa \equiv \sqrt{\kappa_1^2 + \kappa_2^2}$ is the norm of the bending curvature, and $\hat{\mathbf{N}}$ is the normal director of the center-line's Frenet-Serret frame (Fig. 1*C*). Given the average growth rate $\dot{\varepsilon}_g$ and the organ radius R, we connect the change in local intrinsic curvature $\boldsymbol{\kappa}^0(s,t)$ within L_{gz}, to the differential growth $\boldsymbol{\Delta}(s,t)$ projected on the cross-section (30, 41, 42)

$$\dot{\boldsymbol{\kappa}}^0 = \frac{\dot{\varepsilon}_g}{R}\left(\mathbf{d}_3 \times \boldsymbol{\Delta}\right) \qquad [4]$$

as detailed in *SI Appendix*, 2. For simplicity, here we drop the explicit dependence on (s,t). Thus, Eqs. **3** and **4** capture gravitropic dynamics, relating sensing ($\beta\hat{\boldsymbol{g}}$) to differential growth ($\boldsymbol{\Delta}$), which in turn feeds into the root shape ($\boldsymbol{\kappa}^0$). As described in the *Materials and Methods*, $\boldsymbol{\Delta}$ can be rewritten to include different types of internal and external cues, such as phototropism or circumnutations, as well as different sensing profiles (apical and local). Finally, to distill the essential mechanisms underlying the range of observed growth patterns, we neglect the effect of substrate deformations (17, 46), and the coupling between root growth, static friction, and stick-slip dynamics (44, 47, 48). These elements nonetheless deserve future attention.

Some *Arabidopsis* mutants (49–51) exhibit a cell profile which twists during growth (Fig. 4*B*). We model this additional effect by allowing the material frame in the growth zone L_{gz} to twist around the centerline of the organ. This twist is described by an increasing register angle ξ, characterized by the angular velocity at the apex

$$\omega = \frac{\partial \xi}{\partial t} = \tau \dot{\varepsilon}_g L_{gz}, \qquad [5]$$

where τ is a constant intrinsic twist line density (Fig. 4*C*).

Finally, contact forces that prevent the root from penetrating the substrate, and adhesion forces that maintain the mature region

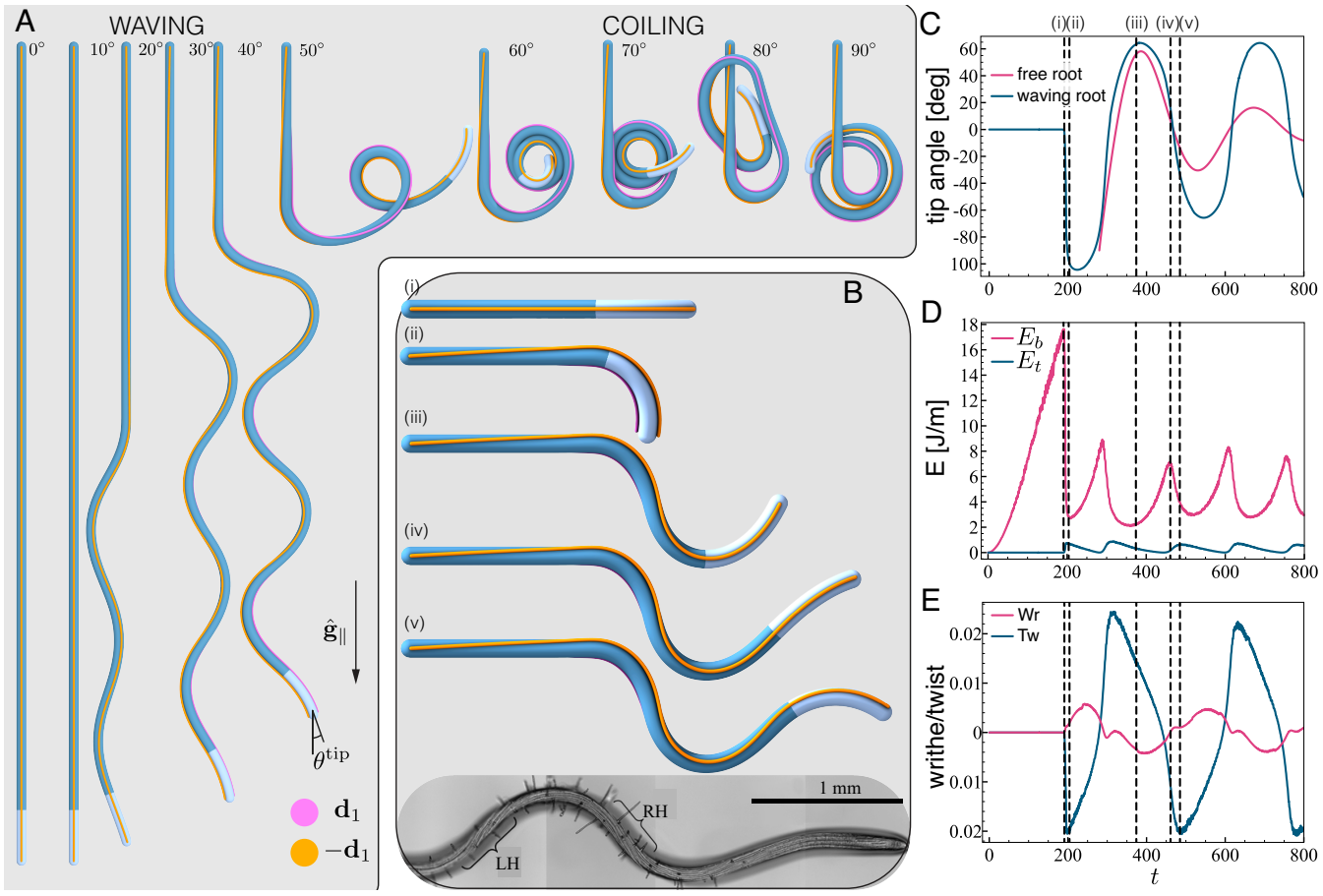

Fig. 2. Simulations reproduce waving and coiling. (*A*) Final configurations. *Top* view of final configurations of simulations for tilt angles $0^0 \le \alpha \le 90^0$, with $\beta = \gamma = 0.1$. Pink and orange lines represent the direction of the vectors $\pm\mathbf{d}_1$ describing the material frame along the organ. The local planar angle $\theta(s,t)$ is the angle between the projection of the organ tangent on the tilted plane, and the projection of the direction of gravity $\hat{\mathbf{g}}_{\parallel}$. (*B*) Snapshots of waving dynamics. Five snapshots during the developing waving pattern for a root at $\alpha = 40^o$, with local gravisensing, $\beta = 0.2$, and $\gamma = 0.1$. Stages (*i*) and (*ii*) depict the first symmetry breaking due to an elastic instability that reduces bending energy by twisting sideways. Between stages (*iii*) and (*v*) left-handed twist is being accumulated in the mature zone as the root turns clock-wise (evident by following $\mathbf{d}_1$), in line with observed twisting cell files (26). (*C*–*E*): Properties of the growth zone during the development of a waving pattern, corresponding to the root in (*B*). Dashed lines represent the snapshots in (*B*), and time is shown in number of time-steps. (*C*) Planar tip angle $\theta^{\text{tip}}(t)$ (blue). For comparison, we show the behavior of a corresponding free organ (pink line), that is of a root growing without substrate but characterized by the same initial angle (with respect to gravity) of the waving root (blue line). Both profiles present oscillations with a similar period; however, in the absence of interactions with the plane, the oscillations decay in time. (*D*) Average elastic bending energy E_b and twisting energy E_t in the growth zone. (*E*) Total writhe Wr and twist Tw in the growth zone.

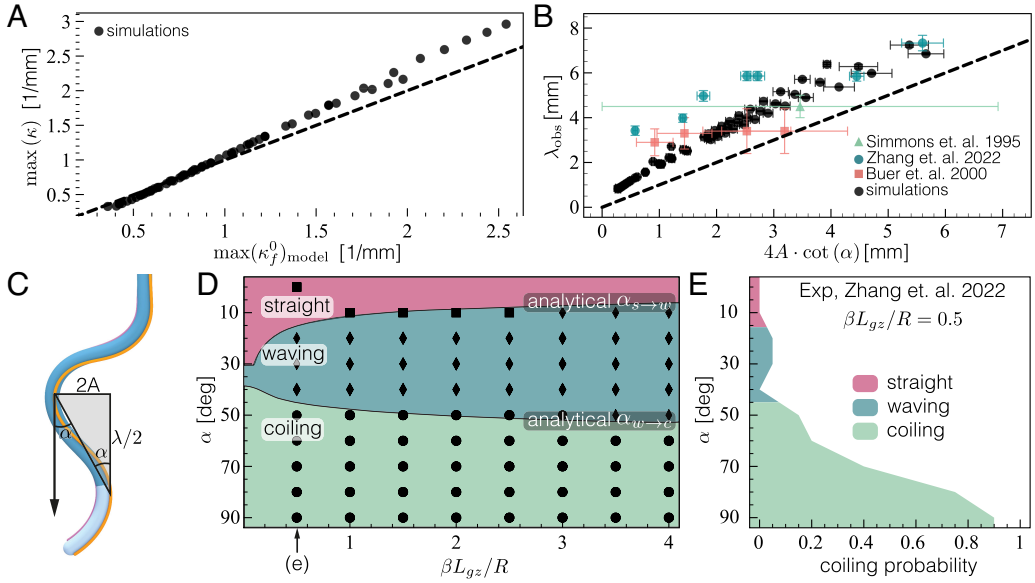

Fig. 3. Comparison of model predictions with simulations and experiments. (*A*) Curvature of waving patterns originate from the gravitropic response of a free organ. The maximal curvature $\max \kappa$ of the projected shape of simulated waving patterns on the plane approximately scales like the predicted maximal curvature of a free organ $\max \kappa_f^0$ (Eq. **8**), tilted at the same angle α, as suggested by Eq. **6**. Simulations were run with $L_{gz}/R = 10$, $\gamma = 0.1$, and $0.05 \leq \beta \leq 1.0$ (Table 1), and for a range of inclinations α. Results for larger values of γ and apical gravisensing are brought in *SI Appendix*, 5. The dashed line represents identity, for reference. (*B*) Wavelength vs. amplitude. Following our proposed scaling laws for the wavelength λ and amplitude A of waving patterns (Eqs. **9**, **10**, and **11**), λ is plotted against $4A\cot(\alpha)$ for values measured in simulations and experiments (16, 46, 63), exhibiting a linear dependence as predicted. The dashed line represents identity, for a reference. The wavelength and amplitude of each simulation are quantified by averaging the distances between neighboring peaks of the waving pattern parallel and normal to the downhill direction. Data points for $\alpha \leq 10$ deg from ref. 46 are not shown as they diverge. (*C*) Geometric relation between wavelength and amplitude. The angle on the plane is the integral over curvature, and following (*A*) is dictated by the tip angle of a free organ, which can be approximated by the inclination angle α (see virtual configuration in Fig. 1*E*). (*D*) Configuration space. Shapes of simulated organs (with $L_{gz}/R = 10$ and $\gamma = 0.1$) for different values of the effective gravitropic gain $\beta L_{gz}/R$ and tilt angle α. Symbols represent the final configuration shape of simulations (■ symbols for straight, ♦ for waving, • for coiling). Simulations agree with model predictions, represented by background color: transitions from straight to waving occur at critical angle $\alpha_{S\to W}$ (Eq. **12**), and transitions to coiling occur at $\alpha_{W\to C}$ (Eq. **13**), estimated in *SI Appendix*, 7. The second column represents the configurations shown in Fig. 2*A*. Equivalent configuration spaces for high γ and apical sensing in *SI Appendix*, 7. (*E*) Observed coiling transition. Experimental observations of coiling probability (46) agree with model prediction (represented by background colors as in (*E*) for $\beta L_{gz}/R = 0.5$). We note that (46) reports probabilities only for the emergence of coiling behavior, with the white portion of the plot encompassing the combined probability of observing straight or waving patterns.

fixed in place (mimicking the effect of root hair attachments and lignification, Fig. 1*A*) are encapsulated in **f**, as detailed in *Materials and Methods* and *SI Appendix*.

Overall, Eqs. **1**–**5** define our model, which we numerically discretize and solve using the open-source software Elastica (54), demonstrated across a range of biophysical problems (55–60) entailing fiber-like structures (*Materials and Methods* and *SI Appendix* 3).

Simulations Recapitulate Waving and Coiling Patterns. Based on waving and coiling experiments (15–21), we simulate *Arabidopsis thaliana* roots growing on a tilted plane for a range of angles α (from vertical to horizontal), as well as gravitropic and proprioceptive gains β and γ. We use parameters and mechanical properties typical of *Arabidopsis* (Table 1 in *Materials and Methods*). For simplicity, we assume frictionless growth while fixing the sessile (mature) zone to the substrate (17, 46), as discussed above. At this stage, we neglect root twisting during growth, although we will revisit it in later sections.

As illustrated in Fig. 2*A* and Movies S1 and S2, simulations capture observed root behavior. Indeed, simulated roots grow straight on a vertical plane ($\alpha = 0$), and transition to waving as the substrate tilt angle reaches $\alpha \approx 15^0$, consistent with experimental measurements (Fig. 1*A*). A further increase in tilt angle initiates a second phase transition, around $\alpha \approx 50^0$, and roots begin to coil, again consistent with experiments (Fig. 1*A*). Transition angles are also consistent with experimental values (46) (Fig. 3*E*), as we shall elaborate later.

To gain intuition about the waving and coiling process, as well as their transitions, we analyze the system from an energetic and topological perspective. Tip dynamics are tracked via the planar angle θ^{tip}. This is the angle between the projections of gravity and the tangent of the apex on the tilted plane (Fig. 2 *A* and *C*). The evolution of the stored energy in the growth zone is described through the approximate elastic bending energy $E_b = \int_{L_{gz}} \boldsymbol{m} \cdot (\delta\kappa_1 \mathbf{d}_1 + \delta\kappa_2 \mathbf{d}_2)\, ds$ and elastic twist energy $E_t = \int_{L_{gz}} \boldsymbol{m} \cdot \delta\kappa_3 \mathbf{d}_3 ds$, where $\delta\boldsymbol{\kappa} = \boldsymbol{\kappa}/\lambda_e - \boldsymbol{\kappa}^0$ and $\boldsymbol{m} = \mathbf{B}\delta\boldsymbol{\kappa}/\lambda_e^2$ (Fig. 2*D*). Additionally, in order to concisely capture root morphology and its reconfigurations, we consider the topological quantities writhe (Wr) and twist (Tw) in the growth zone (Fig. 2*E*). Writhe is computed by treating the growth zone as an open loop (61), and is used here as a measure of out-of-plane bending of the growth zone's centerline. If Wr = 0, then the centerline is in-plane, while positive or negative values of Wr correspond approximately to right- or left-handed out-of-plane bending, respectively (*SI Appendix*, Fig. S2). Twist instead determines the rotation of the local frame around its centerline. Positive and negative values correspond to right-handed and left-handed rotations accordingly (*SI Appendix*, Fig. S2). In a closed or infinitely long rod, the geometric integral quantities Wr and Tw are related topologically, and their sum is constant and constrained by the number of formed loops (62). In our case, their sum is not conserved; however, their topological

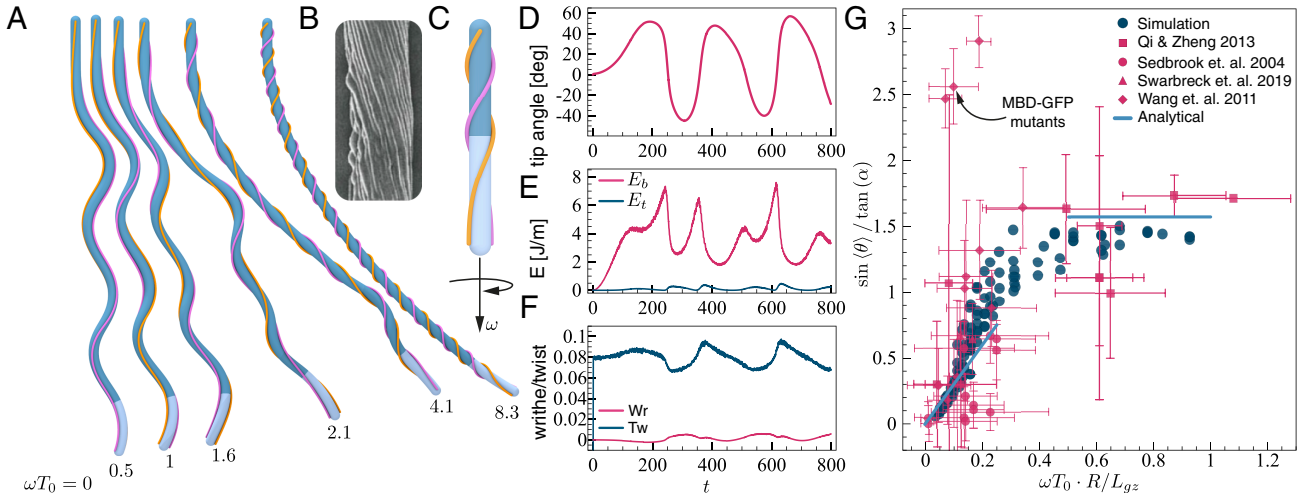

Fig. 4. Simulations and model reproduce skewing patterns. (*A*) Simulation configurations. *Top* view of simulated organs for different twisting frequencies ω and a constant turning time T_0 (with $\alpha = 30^o$, $\gamma = 0.1$, and $\beta = 0.2$). (*B*) Observed cell file rotation of an Arabidopsis mutant exhibiting skewing, manifesting intrinsic twist (50). (*C*) Model for intrinsic twist. The angle between the cell files and the root axis increases from the apex to the mature zone, captured by the angular velocity ω, as described by Eq. **5**. (*D–F*) Properties of the growth zone during the development of a skewed pattern. Similar to Fig. 2 (*C–E*), for $\omega T_0 = 1$. Symmetry is broken by twist, without an elastic instability. A comparison between various values of ωT_0 appears in *SI Appendix*, Fig. S10. (*G*) Relation between skewing angles $\langle\theta\rangle$ and intrinsic twist. Following the limiting relations in Eqs. **14** and **15** we plot $\sin\langle\theta\rangle/\tan\alpha$ vs. $\omega T_0 \cdot R/L_{gz}$, for both simulations and experiments (26, 38, 52, 53). Simulations were run with $L_{gz}/R = 10$, $\gamma = 0.1$, $0.1 \le \beta \le 0.25$, $10^o \le \alpha \le 40^o$, and $0 \le R\tau \le 0.8$, which give $0 \le \omega T_0 \le 9.3$ (Table 1). Experimental data (26, 38, 52, 53) are plotted assuming $L_{gz}\beta/R = 0.5$, and ω is estimated from experimental values of cell file rotation (CFR) via Eqs. **27** and **5**. Predicted asymptotic relations in the limits $\omega T_0 \ll 1$ and $\omega T_0 \gg 1$, as detailed in Eqs. **14** and **15**, are represented by solid lines. Experiments agree with simulations and asymptotic predictions, except for MBD-GFP mutants (26). In *SI Appendix*, Fig. S9, we plot the correlation between intrinsic twist τ and skewing angle $\langle\theta\rangle$ for the experimental data.

connection is useful to qualitatively understand the system dynamics.

As can be seen in Fig. 2*A*, the onset of waving and coiling follows a first turning event. Fig. 2*B* shows snapshots at different stages of a waving organ, animated in Movie S1 and marked for reference in Fig. 2 *C–E*. Snapshot (i) occurs just before the first turning event, where the root grows in a plane defined by its initial tangent and the direction of gravity, as represented by the constant values of θ^{tip} (Fig. 2*C*), Wr and Tw (Fig. 2*E*). Due to gravitropism, the root tends to grow into the substrate (Fig. 1*D*), which in turn resists growth, leading to an increase in bending energy E_b (Fig. 2*D*). This energy is eventually released, breaking symmetry, in the form of an elastic instability—snapshot (ii)—whereby the root tip slips or tilts to one side, bending and twisting. This process is reflected by a sharp drop in E_b accompanied by a jump in all other parameters (Fig. 2 *C–E*). We note that while in simulations this initial symmetry breaking is purely caused by an elastic instability, in experiments a number of factors may further contribute to it, from geometrical or material imperfections to small intrinsic root twists.

We continue to follow the growth of the root during a subsequent turning event. Snapshot (iii) occurs right after the second turn where the tip angle θ^{tip} is at a maximum, and the bending energy E_b is at a minimum. For further insight, it is useful to decompose $\mathbf{\Delta}$ into components parallel and perpendicular to the substrate. The parallel component causes the root to reorient along the projection of gravity on the plane, leading to a decrease in the planar tip angle θ^{tip}. The perpendicular component pushes the apex into the plane, leading again to an increase in E_b, similar to the initial symmetry breaking and in line with observations of substrate deformations (17). As new cells are produced at the tip, older cells stop growing and become part of the mature zone. Thus, accumulated twist leaves the growth zone, so that, at snapshot (iv), E_t reaches a minimum while E_b reaches a maximal value. Then, as for the first bending event, the organ releases bending energy by twisting, and E_b is converted into E_t. This elastic relaxation is accompanied by a conversion of Wr into Tw, since these quantities are topologically related (61). Both E_t and Tw reach a maximum value at snapshot (v). At this point Tw is convected out of the growth zone faster than it is generated, and Tw and E_t decrease. The organ is now back to stage (iii), and the process repeats itself. Since the gravitropic correction of curvature is slower than the elastic relaxation, θ^{tip} repeatedly overshoots in the direction of gravity, producing the observed waving patterns.

We note that our simulations show that neither thigmotropism nor circumnutation is strictly required in order to produce waving and coiling, unlike previously argued (15, 16, 23, 24, 26).

Scaling Analysis. We now perform a scaling analysis of the growth dynamics described in Eqs. **3** and **4**, and relate model parameters to experimentally measurable variables: wavelength λ and amplitude A of root waving patterns, as defined in Fig. 3*C*. Comparing predicted values to experimental measurements will allow to quantitatively corroborate our model. In order to derive relations for amplitude and wavelength, we focus on the curvature of the waving pattern. Simulations (Fig. 2) show that the elastic stresses associated with bending, due to the organ pushing into the substrate, are accumulated until they relax by twisting sideways, which rotates the curvature vector. This suggests that the maximal value of the in-plane curvature of the waving pattern κ, obtained right after twisting, may be comparable to the maximal curvature κ_{f}^0 induced by the gravitropic response in a free organ tilted at the same angle α of the substrate. Thus, we hypothesize that

$$\max \kappa \approx \max \kappa_{\text{f}}^0. \qquad [6]$$

In *SI Appendix*, 6 we provide a detailed analysis supporting this assumption, decomposing the dynamics of a tilted organ into components parallel and perpendicular to the tilted plane. This assumption is also supported by Fig. 2*C*, which compares the

oscillating tip angle of a root waving on a substrate (blue) with the gravitropic bending of a corresponding free organ (pink). This comparison further suggests that the wavelength λ of the waving pattern is dictated by the damped oscillations inherent to the free organ's gravitropic dynamics (64), while the amplitude A is modulated by the mechanical interaction with the substrate.

Therefore, in order to find λ, we first evaluate the characteristic gravitropic turning period T_0, corresponding to the time a tilted free root takes to turn toward the direction of gravity (27, 41). We rewrite Eq. **4** in nondimensional form, assuming $\gamma = 0$ for simplicity, and rescaling length and curvature by L_{gz}, yielding $\frac{d}{dt}(L_{gz}\boldsymbol{\kappa}_f^{\mathbf{0}}) = \dot{\varepsilon}_g \frac{L_{gz}}{R}\beta\,(\mathbf{d}_3 \times \hat{\boldsymbol{g}})$. Values in parentheses are dimensionless, as well as the coefficient $\frac{L_{gz}}{R}\beta$. Since $\mathbf{d}_3$ and $\hat{\boldsymbol{g}}$ are unit vectors, we expect the turning time T_0, related to the rate of change of the normalized curvature $\frac{d}{dt}(L_{gz}\boldsymbol{\kappa}_f^{\mathbf{0}})$, to scale as a function of $\frac{L_{gz}}{R}\beta$, with $1/\dot{\varepsilon}_g$ the overall timescale of the problem. Based on free organ's simulations (*SI Appendix*, 5) we find

$$T_0 \sim \frac{\pi}{2}\frac{1}{\dot{\varepsilon}_g}\left(\frac{L_{gz}}{R}\beta\right)^{-3/5}. \qquad [7]$$

Here L_{gz}/R is the geometric slenderness ratio of the growth zone, and we interpret $\frac{L_{gz}}{R}\beta$ as an effective gravitropic sensitivity (64). We approximate $\max\kappa_f^0 \sim T_0 \max d\kappa_f^0/dt$ and substitute $d\kappa_f^0/dt$ from Eq. **4** (with $\gamma = 0$) to obtain

$$\max\kappa_f^0 \sim T_0\frac{\dot{\varepsilon}_g}{R}\beta\sin\alpha. \qquad [8]$$

This equation provides an estimate for $\max\kappa_f^0$, which together with Eq. **6** relates the waving curvature to the gravitropic curvature. In Fig. 3*A*, we validate Eq. **6** for a range of tilt angles by plotting $\max\kappa$, the maximal curvature measured from simulated waving patterns, against $\max\kappa_f^0$, the analytically predicted maximal curvature for a free tilted organ in Eq. **8**, finding good quantitative agreement.

Having verified that the timescale of the waving pattern is related to the gravitropic bending, we can approximate the length $\lambda/2$ grown during a turning event (Fig. 3*C*) as

$$\frac{\lambda}{2} \approx T_0 v_g^{\mathrm{tip}}, \qquad [9]$$

where v_g^{tip} is the tip growth speed. Then, following simple geometric arguments, we relate the amplitude A to the wavelength. After a turn event, $2A$ and $\lambda/2$ form an orthogonal triangle (Fig. 3*C*). Based on Eq. **6**, and since in the gravitropic response of a free organ the angle between the base and the tip is equal to the tilt angle α (Fig. 1*D*), we can infer

$$2A \approx T_0 v_g^{\mathrm{tip}}\tan(\alpha). \qquad [10]$$

By combining Eqs. **9** and **10**, we then obtain

$$\lambda \approx 4A\cot(\alpha) \qquad [11]$$

directly relating wavelength λ and amplitude A through the incline α. We compare Eq. **11** with simulations and experiments (16, 46, 63) in Fig. 3*B*, noting consistent trends. The individual scaling relations (Eqs. **9** and **10**) are also tested in *SI Appendix*, 5. Throughout, we assume local sensing. We additionally report results for apical sensing in *SI Appendix*, 5 (*Materials and Methods*), observing no qualitative differences.

Transitions between Straight, Waving and Coiling. Here, we provide an intuitive rationale for the two critical tilt angles at which the root transitions from straight to waving ($\alpha_{s\to w}$) and from waving to coiling ($\alpha_{w\to c}$), with the full derivation reported in *SI Appendix*, 7.

Simulations of Fig. 2 suggest that waving patterns are initiated by an elastic instability, which occurs when it becomes energetically convenient to twist rather than to bend, i.e. $E_t < E_b$. Again assuming that the intrinsic curvature is captured by the gravitropic response of the free organ $\max\kappa_f^0$ (Eq. **8**), before the turn we can approximate $E_b \propto (\max\kappa_f^0)^2$. The accumulated angle during the gravitropic response is roughly equal to the tilt angle $L_{gz}\max\kappa_f^0 \approx \alpha$, meaning that E_b increases with the tilt angle. However, E_t is constant, and at a critical angle $\alpha_{s\to w}$ the two energies intersect $E_t = E_b(\alpha_{s\to w})$ and waving occurs. The critical angle (detailed in *SI Appendix*, 7) follows

$$\sin(\alpha_{s\to w}) = \sqrt{\frac{2}{3}}\frac{2\Delta\xi}{\pi}\left(\frac{\beta L_{gz}}{R}\right)^{-\frac{2}{5}}, \qquad [12]$$

where $\Delta\xi$ is a fitting parameter representing the change in the register angle ξ created by the integrated elastic twist (Fig. 1*C*).

The transition between waving and coiling is instead related to the ratio between i) the time to turn toward gravity after a twist-induced relaxation and ii) passive orientation drift (27)—the rate at which the tip angle of a curved organ increases due to growth, maintaining the same curvature, thus reorienting growth uphill in this case. The former is proportional to the amplitude of the waving pattern $T_0\tan(\alpha)$ in Eq. **10**, and the latter follows $T_{dr} \approx 1/(\dot{\varepsilon}_g L_{gz}\max\kappa)$ (27). At at a critical angle $\alpha_{w\to c}$ orientation drift occurs faster than turning, $T_{dr} < CT_0\tan(\alpha)$, and coiling ensues. The coiling critical angle (detailed in *SI Appendix*, 7) then follows

$$\frac{\sin^2(\alpha_{w\to c})}{\cos(\alpha_{w\to c})} = \frac{4}{C\pi^2}\left(\frac{\beta L_{gz}}{R}\right)^{\frac{1}{5}}, \qquad [13]$$

where C is a fitting parameter.

We corroborate the predicted critical angles both numerically and experimentally. Fig. 3*D* shows the configuration space of simulated organs over a range of α and effective gravitropic bending $\beta L_{gz}/R$ (where for *Arabidopsis* roots we use 0.5, see Table 1). For each set of parameters, we compare the conformation observed in simulations (■ symbols for straight, ♦ for waving, • for coiling) to the predicted one (represented by background colors, separated by the critical angles), with $\Delta\xi = \pi/8$ and $C = 0.5$, finding good agreement. Configuration spaces for cases with $\gamma = 1$, and apical sensing, can be found in *SI Appendix*, 7, where we note no qualitative difference. In Fig. 3*E* we also compare our results to the coiling probability measured in vivo by Zhang et al. (46), again finding good quantitative agreement.

Intrinsic Twist Yields Skewing Patterns. Last, we focus on the skewed waving patterns observed in some *Arabidopsis* mutants (26, 38, 52, 53) (Fig. 1*A*). Observations suggest that the skewing angle is related to the twisting of root cell files (Fig. 4*B*), which may be represented as an intrinsic twist of the material frame around the centerline of the growth zone, as described in Eq. **5** and detailed in the *Materials and Methods* (Fig. 4*C*). When accounting for such rotations (ω in Eq. **5**), simulations recover observations of skewing (Fig. 4*A* and Movies S3–S5). We see how increasing the ratio between the bending time and the twisting velocity, ωT_0, results in larger skewing angles and

washes out the waving pattern. This is reflected in the evolution of energetic and topological variables: $\omega T_0 = 1$ (Fig. 4 *D–F*) exhibits oscillatory behavior similar to that of regular waving patterns, while $\omega T_0 = 8.3$ (*SI Appendix*, Fig. S10) transitions to a more monotonic behavior. Here, the initial breaking of symmetry manifests as a smooth, twist-induced rotation, facilitated by the intrinsic cell file rotation (26). We also note that circumnutations are not required; however, they could have a secondary role, as we find that with no intrinsic twist circumnutations lead to disordered patterns and low skewing angles (*SI Appendix*, 8), explaining observed coiling in agravitropic roots (16).

Next, we relate the average skewing angle $\langle\theta\rangle$ (defined in Fig. 2*A*) to ω, for two limiting cases. When $\omega T_0 \ll 1$, the apical rotation due to intrinsic twist acts as a small perturbation to the waving mechanism, accelerating turns in the same direction, while slowing down opposite turns (Fig. 4 *D–F*). Thus, the amplitude of the turn increases in one direction, $A_+ \approx A(1 + \omega T_0)$, and decreases in the other, $A_- \approx A(1 - \omega T_0)$. From trigonometric arguments $\sin\langle\theta\rangle$ is the horizontal displacement due to the difference in amplitude over two turns, divided by the wavelength $\sin\langle\theta\rangle \approx \Delta A/\lambda$, with $\Delta A = 2A_+ - 2A_- = 4A\omega T_0$. Substituting the expressions for λ and A in Eqs. **9**–**10** yields

$$\lim_{\omega T_0 \ll 1} \sin\langle\theta\rangle \approx \omega T_0 \tan\alpha. \quad [14]$$

In the opposite limit $\omega_0 T_0 \gg 1$, the twist-induced rotation dominates, and the waving pattern disappears altogether. Following simple geometric arguments (Fig. 1*D*), the skewing angle $\langle\theta\rangle$ reduces the in-plane gravitropic component $\beta_\parallel = \beta \cos\alpha \sin\langle\theta\rangle$; however, it does not affect the perpendicular component directed into the plane, $\beta_\perp = \beta \sin\alpha$, which causes the apex to drift uphill when twisted into the plane. The constant skewing angle suggests that these two competing processes balance each other, $\beta_\perp = \beta_\parallel$, yielding

$$\lim_{\omega T_0 \gg 1} \sin\langle\theta\rangle \approx \tan\alpha. \quad [15]$$

We corroborate our skewing model (limiting relations Eqs. **14** and **15** and simulations) against experimental observations (26, 38, 52, 53) in Fig. 4*G*. As can be seen, theory and simulations are found to be consistent among themselves as well as able to capture general trends across a variety of *Arabidopsis* mutants. Only a particular strain, expressing MBD-GFP (26), is found to significantly depart from our predictions (*Top/Left* corner of Fig. 4*G*). While we cannot comment on the effect of this specific mutation on growth behavior, we note that these outliers are themselves a subset of the specimens investigated in ref. 26, which are otherwise in agreement with all data of Fig. 4*G*.

Conclusions

We developed a numerical framework for simulating the interaction of plant roots with solid interfaces, integrating passive mechanics and active growth-driven mechanics. Our methods are shown to reproduce the range of growth patterns exhibited by *Arabidopsis* roots grown on a tilted plane, a well-documented biophysical plant model. Our simulations illustrate how the interplay between active gravitropic response and passive elasticity are the minimal requirements to generate straight, waving, and coiling patterns, while the addition of intrinsic twist is responsible for skewing. We find that neither thigmotropism nor circumnutation are required to recover waving or skewing patterns, as previously argued (16, 23–25); however, they could play a secondary role.

A scaling analysis reveals that the amplitude of waving patterns is modulated by the mechanical interaction with the substrate, while the wavelength depends on oscillations inherent to the gravitropic dynamics of a free organ, regardless of the interaction with the plane. Based on this analysis we develop analytical expressions for the critical tilt angles for which the root behavior transitions from straight to waving and then coiling. Further, we elucidate the relation between skewing angles and intrinsic twist. We corroborate all these analytical insights by comparing model predictions to both simulations and experimental observations, obtaining good agreement.

This framework provides, effectively, an in silico laboratory to form and test hypotheses relative to the behaviors of plants and their mechano-sensory machinery in realistic environments. Future extensions will consider heterogeneous terrain via the inclusion of granular mechanics. Finally, we note that since our approach is general and agnostic to the underlying biological building blocks, it can be applied to growth-driven systems other than plant organs, such as neurons, fungal hyphae, or new generation of growing robots (65–68).

Materials and Methods

Here, we consider a plant organ as a slender rod, whose centerline is parameterized by s, with $s = 0$ at the base and $s = l$ at the tip, l being the organ length (Fig. 1*B*). In order to describe its dynamics, we assume a separation of timescales between slow growth-driven processes and fast elastic relaxation (28, 29). At each time step of our integration scheme, we first update the configuration of the organ according to the growth process alone, and then allow it to relax mechanically following Cosserat rod theory (37) (Fig. 1*D*). For the sake of clarity, the intermediate stress-free configuration is parameterized with S, in order to differentiate it from the final relaxed configuration described with s. The initial configuration is marked with S_0. In what follows, we bring the governing equations describing the growth dynamics and the mechanical relaxation.

Shape. At each point s along the centerline we define the position vector $\boldsymbol{r}(s,t)$, which provides the 3D description of the rod at time t (Fig. 1*B*). We also define a local orthonormal material frame $\{\mathbf{d}_1(s,t), \mathbf{d}_2(s,t), \mathbf{d}_3(s,t)\}$, where $\mathbf{d}_1$ and $\mathbf{d}_2$ span the cross-section of the organ, and in a shearless and inextensible system $\mathbf{d}_3$ coincides with the tangent of the centerline. The local curvature vector $\boldsymbol{\kappa}(s,t)$ (or Darboux vector) of the center-line is defined through the relation $\frac{\partial \mathbf{d}_i(s,t)}{\partial s} = \boldsymbol{\kappa}(s,t) \times \mathbf{d}_i(s,t)$ (37). The components of curvature projected along the principal vectors of the material frame ($\boldsymbol{\kappa} = \kappa_1\mathbf{d}_1 + \kappa_2\mathbf{d}_2 + \kappa_3\mathbf{d}_3$) coincide with bending (κ_1, κ_2) and twist (κ_3) strains in the material frame. Introducing elastic stretch may lead to a difference between the arc-length configuration s and the stress-free configuration S, described by the local stretch (37) $\lambda_e(s,t) = \frac{\partial s}{\partial S}$. Shear may leads to an incongruity between $\mathbf{d}_3$ and the tangent of the centerline, and the local deviation is described by the translation vector $\boldsymbol{\sigma}(s,t) = \lambda_e(s,t)\frac{\partial \boldsymbol{r}(s,t)}{\partial s} - \mathbf{d}_3(s,t)$ (Fig. 1*B*).

Growth. Root growth occurs in the growth zone, an area of length L_{gz} just below the root tip. Cells divide at the tip, and elongate within the growth zone, until stop elongating and reach the mature zone (Fig. 1*E*). The initial configuration then represents the material (or Lagrangian) coordinate which flows due to growth with velocity v_g, which is the integral of the mean axial relative growth rate $\dot{\varepsilon}_g \geq 0$

$$v_g(S,t) = \dot{S}(S_0,t) = \int_0^S \dot{\varepsilon}_g(u,t)du. \quad [16]$$

Here the growth rate is the time derivative of the logarithmic growth strain $\varepsilon_g = \ln\lambda_g$, where $\lambda_g \equiv \frac{\partial S}{\partial S_0}$ is the growth stretch. The increase in rest lengths enters the dynamics via the actual and intrinsic stretch vectors, defined

as $\boldsymbol{\sigma} = \left(\lambda_e \frac{\partial \boldsymbol{r}}{\partial s} - \lambda_g \mathbf{d}_3\right)$ and $\boldsymbol{\sigma}^0 = -\left(\lambda_g - 1\right)\mathbf{d}_3$ respectively, such that $\boldsymbol{\sigma} - \boldsymbol{\sigma}^0 = \left(\lambda_e \frac{\partial \boldsymbol{r}}{\partial s} - \mathbf{d}_3\right)$. As described in the main text, growth-driven movements are generally classified into tropic and nastic movements, where the former are due to external stimuli, such as gravitropism, and the latter are due to internal cues, such as the oscillatory movements of circumnutations. Changes in curvature are due to the anisotropic redistribution of growth hormones, leading to asymmetric growth along the cross-section captured by the differential growth vector $\boldsymbol{\Delta}(s,t)$ (30). The dynamics resulting change in intrinsic curvature $\boldsymbol{\kappa}^0$ for $L(t) - L_{gz} \le s \le L(t)$ within the growth zone follows (30)

$$\dot{\boldsymbol{\kappa}}^0 = \frac{\dot{\varepsilon}_g}{R}(\mathbf{d}_3 \times \boldsymbol{\Delta}). \qquad [17]$$

Here $\dot{\boldsymbol{\kappa}}^0 = \frac{\partial \boldsymbol{\kappa}^0}{\partial t} + v_g \frac{\partial \boldsymbol{\kappa}^0}{\partial s} \equiv \frac{D\boldsymbol{\kappa}^0}{Dt}$ is a material derivative which accounts for the growth of the centerline. For simplicity, we assume no intrinsic twist, $\kappa_3^0 = 0$. The cross-product $\mathbf{d}_3 \times \boldsymbol{\Delta}$ represents a projection of $\boldsymbol{\Delta}$ on the local cross-section of the organ (details in *SI Appendix*, 2). The tropic and nastic movements then contribute to the total differential growth vector $\boldsymbol{\Delta}$. In the case of gravitropism, we have

$$\boldsymbol{\Delta}_g(s,t) = \beta \mathbf{R}(s,t)\hat{\boldsymbol{g}} - \gamma R \kappa(s,t)\hat{\mathbf{N}}(s,t). \qquad [18]$$

The first term represents the gravity stimulus, with $\hat{\boldsymbol{g}}$ the direction of gravity and β the gravitropic sensitivity or gain reflecting the variance in the magnitude of gravitropic responses across different species (41). The second term represents proprioception which can be thought of as a counter-curving response (41), where γ is its gain, R is the radius of the organ, $\kappa \equiv \sqrt{\kappa_1^2 + \kappa_2^2}$ is the norm of the bending curvature, and $\hat{\mathbf{N}}$ is the normal director of the Frenet-Serret frame. The matrix $\mathbf{R}(s,t)$ in the gravitropic term represents the sensing mechanism: in the case of local sensing used here $\mathbf{R}(s,t) = \mathbf{I}$, and in the case of apical sensing where sensing occurs at the tip alone we set $\mathbf{R}(s,t) = \mathbf{Q}(s,t)\mathbf{Q}^T(l(t),t)$. This rotation matrix takes vectors from the material frame at the apex, $s = l(t)$, to points along the growth zone s, and assures that the directional signal sensed at the apex is instantaneously transferred to every arc-length s. Results of simulations with apical sensing are described in *SI Appendix*, 5 and 7. We model circumnutations as resulting from differential growth rotating around the center-line without introducing twist (30, 31, 33, 42)

$$\boldsymbol{\Delta}_{CN} = \lambda\left(\cos(\Omega t)\hat{\mathbf{m}}_1 + \sin(\Omega t)\hat{\mathbf{m}}_2\right), \qquad [19]$$

where λ is the circumnutation gain, Ω is its temporal angular frequency and $\hat{\mathbf{m}}_1$ and $\hat{\mathbf{m}}_2$ are unit vectors of a normal development of the centerline (30). We assume that the two processes are additive, allowing to take $\boldsymbol{\Delta} = \boldsymbol{\Delta}_{CN} + \boldsymbol{\Delta}_g$.

Adding a Twisting Material Frame. Various *Arabidopsis* mutants exhibiting skewing angles also seem to exhibit a twisting cell profile (49–51), which can be interpreted as a twisting material frame around the centerline of the organ, described by the relative angle $\xi \equiv \arccos(\hat{\mathbf{m}}_1 \cdot \mathbf{d}_1)$ (Fig. 1*C*). Based on experimental observations, we chose a twist profile where the angle between the cell files and the root axis increases from the apex, where it is zero, to the mature zone where it reaches a constant value (Fig. 4 *B* and *C*). This is implemented using a linear profile for the arc-length derivative of ξ

$$\frac{\partial \xi(S,t)}{\partial S} = \begin{cases} \tau - \frac{\tau}{L_{gz}}\left(S - (L(t) - L_{gz})\right) & S \in \mathrm{GZ} \\ \tau & S \in \mathrm{MZ} \end{cases} \qquad [20]$$

with GZ is the growth zone $L(t) - L_{gz} \le S \le L(t)$, and MZ is the mature zone $0 \le S < L(t) - L_{gz}$, where $L(t)$ is the length of the organ and L_{gz} is the length of the growth zone. Here τ represents twist, where a positive or negative value represents a right or left-handed twist respectively. The intrinsic angle between the cell files and the root axis is $\arctan\left(R\frac{\partial \xi}{\partial S}\right)$ with a maximal value in the mature zone of $\arctan(R\tau)$. The angular frequency of rotation of the tissue at the tip follows $\omega = \partial \xi(L(t),t)/\partial t = \tau \dot{\varepsilon}_g L_{\mathrm{gz}}$ clockwise (looking from the base to the apex, see Fig. 4*C*). When incorporating twist into the dynamics of Eq. **4**, only the component in the direction of $\mathbf{d}_3$ is affected, reading

$$\dot{\kappa}_3^0(S,t) = \frac{d}{dt}\frac{\partial}{\partial S}\xi(S,t). \qquad [21]$$

See more details in *SI Appendix*, 2.

Mechanics. Mechanical equilibrium is achieved at each time step when the time-independent Cosserat rod equations are fulfilled along the centerline (37)

$$\frac{\partial \boldsymbol{n}}{\partial s} + \boldsymbol{f} = 0, \qquad [22]$$

$$\frac{\partial \boldsymbol{m}}{\partial s} + \frac{\partial \boldsymbol{r}}{\partial s} \times \boldsymbol{n} + \boldsymbol{c} = 0, \qquad [23]$$

where $\boldsymbol{n}$ are the internal contact forces, $\boldsymbol{\tau}$ are the internal torques or bending moments, $\boldsymbol{f}$ are the external forces per unit length and $\boldsymbol{c}$ are the external couples per unit length, all functions of s and t. The full elastic relaxation dynamics of the second step are based on the Cosserat model with a dissipation mechanism, as described in ref. 37 and *SI Appendix*, 3B. We follow (37) and choose a constitutive model that assumes linear elasticity, namely the internal contact forces are linearly related to the shear and stretch of the centerline, and the internal torques are linearly related to the bending and twisting

$$\boldsymbol{n} = \mathbf{S}\left(\boldsymbol{\sigma} - \boldsymbol{\sigma}^0\right) = \mathbf{S}\left(\lambda_e \frac{\partial \boldsymbol{r}}{\partial s} - \mathbf{d}_3\right), \qquad [24]$$

$$\boldsymbol{m} = \mathbf{B}\left(\boldsymbol{\kappa} - \boldsymbol{\kappa}^0\right), \qquad [25]$$

where $\mathbf{S}$ and $\mathbf{B}$ are stiffness matrices which are related to the cross-sectional area and the second moment of inertia and are therefore diagonal in the local material coordinates. We also assume volume conservation, varying the local radius of the organ in order to compensate for the elastic stretch $R \to R/\sqrt{\lambda_e(s,t)}$.

Simulating *Arabidopsis thaliana* rRoots. We simulate classic waving experiments on *Arabidopsis thaliana*, placing a rod on a plane tilted at an angle α with respect to the vertical (see Fig. 1*D*), allowing it to grow during 1,500 to 3,000 growth time-steps, which increases their length by a factor of 15 to 30. We adopt values for *Arabidopsis thaliana*, taking the radius $R = 0.1$mm (43, 64), and an initial length $L_0 = 1.1$mm (see Table 1). We assume that growth is restricted to a sub-apical growth zone of length L_{gz}, such that $\dot{\varepsilon}_g(s,t) = \dot{\varepsilon}_g^0$ within the growth zone $L(t) - L_{gz} \le S \le L(t)$, and $\dot{\varepsilon}_g(s,t) = 0$ elsewhere (8) (Fig. 1 *B* and *E*). According to Eq. **16**, the maximal growth velocity at the tip is $v_g^{\mathrm{tip}} = \dot{\varepsilon}_g^0 L_{gz}$, so that $L(t) = L_0 + \dot{\varepsilon}_g^0 L_{gz} t$. In our simulations we take $L_{gz} = 1$mm and $\dot{\varepsilon}_g^0 = 0.2\mathrm{h}^{-1}$ following experimental data (43). We assume the roots are incompressible with an effective Poisson's ratio of 0.5 and Young's modulus of $E = 50$ MPa (8, 69), yielding the stiffness matrices $\mathbf{S} = E\pi R^2 \cdot \mathrm{diag}(8/9, 8/9, 1)$ and $\mathbf{B} = E\pi R^4 \cdot \mathrm{diag}(1/4, 1/4, 1/6)$, expressed in the local material frame (37). Values are summarized in Table 1. We assume the plane is frictionless. In order to emulate the stiff agar surface we assume the

Table 1. Parameters used to emulate *Arabidopsis thaliana* roots

Parameter	Value used	Units
R	100	μm
L_{gz}	1	mm
$\dot{\varepsilon}_g^0$	0.2	1/h
E	50	MPa
β	0.05 to 1.0	
γ	0.0 to 10.0	
$R\tau$	0.0 to 0.8	
$v_g^{\mathrm{tip}} = \dot{\varepsilon}_g^0 L_{gz}$	0.2	mm/h
$\beta L_{gz}/R$	0.5	

The values taken have the same order of magnitude as their measured values, as described in refs. 8, 27, 43, 64, 69. The values for $R\tau$ are chosen based on data from refs. 23, 26, 38, 52, 53 and Eq. **27** as plotted in *SI Appendix*, 9. The last relation was used in order to fit experimental data in Fig.4.

plane applies a local normal restoring force with a spring constant of 100 kg/s^2 and dissipative damping of the normal velocity with a dissipation coefficient of 0.01 kg/s for more details see ref. 37. The mature zone adheres to the substrate due to development of root hairs and lignification (8), which we emulate by using a restoring force with a spring constant of 1,000 kg/s^2 which fixes in place material that exists the growth zone. Thus only the growth zone is free to change its form, while the mature zone is only free to twist around its axis. We vary the gravitropic sensitivity between $0.05 \leq \beta \leq 1.0$ following experimental observations (43), and vary proprioceptive sensitivity in the range $0 \leq \gamma \leq 10$ (27), though its role in roots hasn't been established as clearly as in shoots (64).

Solver Validation. We validate our solver in *SI Appendix*, 3 by comparing our simulations to two analytically solvable cases: i) a clamped organ growing in the direction of an obstacle until it buckles , and ii) the tropic response to a constant stimulus in the case of apical sensing. In *SI Appendix*, 3, we also provide additional information regarding the numerical discretization of growth, and a numerical criterion for mechanical equilibrium. For more details about Elastica and the implementation of interactions between the rod and external obstacles see refs. 37 and 54.

Estimation of Intrinsic Twist Profile. The intrinsic twist can be evaluated by counting the number of epidermal cells that cross a line tangent to the root axis, yielding the parameter CFR (cell file rotation) such that [CFR] = Number/length. The average projected length of one epidermal cell on the root axis is therefore 1/CFR. Assuming that a cell's width is $w \approx 0.01$ mm (51), we can estimate the angle of the cell file with respect to the root axis by

$$\sin(\eta) = \mathrm{CFR} \cdot w. \quad [26]$$

This angle in the mature zone can be expressed using $\eta = \arctan(\tau \cdot R)$, and we estimate τ from the CFR following

$$\tau \approx \frac{1}{R}\tan(\arcsin(\mathrm{CFR} \cdot w)) = \frac{1}{R}\frac{\mathrm{CFR} \cdot w}{\sqrt{1-(\mathrm{CFR} \cdot w)^2}}. \quad [27]$$

Data, Materials, and Software Availability. All study data are included in the article and/or supporting information.

ACKNOWLEDGMENTS. We thank Ido Regev for helpful conversations, and for providing the experimental data from Zhang et al. (2022), used in Fig. 3. Y.M. acknowledges funding from: Israel Science Foundation Grant (1981/14); European Union's Horizon 2020 research and innovation program under Grant Agreement No. 824074 (GrowBot); Human Frontier Science Program, Reference No. RGY0078/2019. M.G. acknowledges funding from: NSF CAREER #1846752, ONR MURI N00014-19-1-2373, NSF EFRI C3 SoRo #1830881, NSF CSSI #2209322, NSF Expedition "Mind in Vitro" #IIS–2123781, with computational support provided through allocation TG-MCB190004 from the Extreme Science and Engineering Discovery Environment (XSEDE; NSF grant ACI-1548562).

Author affiliations: [a]Department of Condensed Matter, School of Physics and Astronomy, Tel Aviv University, Tel Aviv 69978, Israel; [b]Center for Physics, Chemistry of Living Systems, Tel-Aviv University, Tel Aviv 69978, Israel; [c]Mechanical Sciences and Engineering, University of Illinois at Urbana–Champaign, Urbana, IL 61801; and [d]Faculty of Life Sciences, School of Plant Sciences and Food Security, Tel Aviv University, Tel Aviv, Israel

1. L. Taiz, E. Zeiger, *Plant Physiology* (Sinauer Associates, 2010).
2. C. J. Stubbs, D. D. Cook, K. J. Niklas, A general review of the biomechanics of root anchorage. *J. Exp. Bot.* **70**, 3439–3451 (2019).
3. J. Gliński, J. Lipiec, *Soil Physical Conditions and Plant Roots* (CRC Press, 2018).
4. L. Dupuy, T. Fourcaud, A. Stokes, A numerical investigation into the influence of soil type and root architecture on tree anchorage. *Plant Soil* **278**, 175–189 (2007).
5. S. Gilroy, P. Masson, *Plant Tropisms* (Wiley-Blackwell, 2007).
6. L. W. F. Muthert, L. G. Izzo, M. van Zanten, G. Aronne, Root tropisms: Investigations on earth and in space to unravel plant growth direction. *Front. Plant Sci.* **10**, 1807 (2020).
7. J. A. Lockhart, An analysis of irreversible plant cell elongation. *J. Theor. Biol.* **8**, 264–275 (1965).
8. E. Kolb, V. Legué, M. B. Bogeat-Triboulot, Physical root-soil interactions. *Phys. Biol.* **14**, 065004 (2017).
9. J. L. Silverberg *et al*., 3D imaging and mechanical modeling of helical buckling in *Medicago truncatula* plant roots. *Proc. Natl. Acad. Sci. U.S.A.* **109**, 16794–16799 (2012).
10. W. Jin *et al*., Modeling root system growth around obstacles. *Sci. Rep.* **10**, 1–16 (2020).
11. D. C. Trinh *et al*., How mechanical forces shape plant organs. *Curr. Biol.* **31**, R143–R159 (2021).
12. K. Jin *et al*., How do roots elongate in a structured soil? *J. Exp. Bot.* **64**, 4761–4777 (2013).
13. L. X. Dupuy *et al*., Micromechanics of root development in soil. *Curr. Opinion Genet. Dev.* **51**, 18–25 (2018).
14. K. Jonsson, Y. Ma, A. L. Routier-Kierzkowska, R. P. Bhalerao, Multiple mechanisms behind plant bending. *Nat. Plants* **9**, 13–21 (2023).
15. K. Okada, Y. Shimura, Reversible root tip rotation in *Arabidopsis* seedlings induced by obstacle-touching stimulus. *Science* **250**, 274–276 (1990).
16. C. Simmons, D. Söll, F. Migliaccio, Circumnutation and gravitropism cause root waving in *Arabidopsis thaliana*. *J. Exp. Bot.* **46**, 143–150 (1995).
17. M. V. Thompson, N. M. Holbrook, Root-gel interactions and the root waving behavior of *Arabidopsis*. *Plant Physiol.* **135**, 1822–1837 (2004).
18. M. Oliva, C. Dunand, Waving and skewing: How gravity and the surface of growth media affect root development in *Arabidopsis*. *New Phytol.* **176**, 37–43 (2007).
19. J. C. Sedbrook, D. Kaloriti, Microtubules, maps and plant directional cell expansion. *Trends Plant Sci.* **13**, 303–310 (2008).
20. F. Migliaccio, A. Fortunati, P. Tassone, Arabidopsis root growth movements and their symmetry: Progress and problems arising from recent work. *Plant Signal. Behav.* **4**, 183–190 (2009).
21. R. Roy, D. C. Bassham, Root growth movements: Waving and skewing. *Plant Sci.* **221**, 42–47 (2014).
22. T. H. Tan *et al*., How grow-and-switch gravitropism generates root coiling and root waving growth responses in *Medicago truncatula*. *Proc. Natl. Acad. Sci. U.S.A.* **112**, 12938–12943 (2015).
23. R. Rutherford, P. H. Masson, *Arabidopsis thaliana sku* mutant seedlings show exaggerated surface-dependent alteration in root growth vector. *Plant Physiol.* **111**, 987–998 (1996).
24. J. L. Mullen *et al*., Root-growth behavior of the *Arabidopsis* mutant rgr1: Roles of gravitropism and circumnutation in the waving/coiling phenomenon. *Plant Physiol.* **118**, 1139–1145 (1998).
25. A. A. Sipos, P. L. Várkonyi, A unified morphoelastic rod model with application to growth-induced coiling, waving, and skewing of plant roots. *J. Mech. Phys. Solids*, 104789 (2022).
26. Y. Wang, B. Wang, S. Gilroy, E. W. Chehab, J. Braam, CML24 is involved in root mechanoresponses and cortical microtubule orientation in *Arabidopsis*. *J. Plant Growth Regul.* **30**, 467–479 (2011).
27. R. Bastien, S. Douady, B. Moulia, A unifying modeling of plant shoot gravitropism with an explicit account of the effects of growth. *Front. Plant Sci.* **5**, 136 (2014).
28. R. Chelakkot, L. Mahadevan, On the growth and form of shoots. *J. R. Soc. Interface* **14**, 20170001 (2017).
29. A. Goriely, *The Mathematics and Mechanics of Biological Growth* (Springer, 2017).
30. A. Porat, F. Tedone, M. Palladino, P. Marcati, Y. Meroz, A general 3D model for growth dynamics of sensory-growth systems: From plants to robotics. *Front. Robot. AI* **7**, 89 (2020).
31. D. Agostinelli, A. Lucantonio, G. Noselli, A. DeSimone, Nutations in growing plant shoots: The role of elastic deformations due to gravity loading. *J. Mech. Phys. Solids* **136**, 103702 (2020).
32. D. E. Moulton, T. Lessinnes, A. Goriely, Morphoelastic rods III: Differential growth and curvature generation in elastic filaments. *J. Mech. Phys. Solids* **142**, 104022 (2020).
33. D. E. Moulton, H. Oliveri, A. Goriely, Multiscale integration of environmental stimuli in plant tropism produces complex behaviors. *Proc. Natl. Acad. Sci. U.S.A.* **117**, 32226–32237 (2020).
34. A. Bressan, M. Palladino, W. Shen, Growth models for tree stems and vines. *J. Differ. Eq.* **263**, 2280–2316 (2017).
35. T. Guillon, Y. Dumont, T. Fourcaud, A new mathematical framework for modelling the biomechanics of growing trees with rod theory. *Math. Comput. Model.* **55**, 2061–2077 (2012).
36. O. E. Jensen, A field theory for plant tropisms (2021).
37. M. Gazzola, L. Dudte, A. McCormick, L. Mahadevan, Forward and inverse problems in the mechanics of soft filaments. *Roy. Soc. Open Sci.* **5** (2018).
38. J. C. Sedbrook, D. W. Ehrhardt, S. E. Fisher, W. R. Scheible, C. R. Somerville, The *Arabidopsis* SKU6/SPIRAL1 gene encodes a plus end-localized microtubule-interacting protein involved in directional cell expansion. *Plant Cell* **16**, 1506–1520 (2004).
39. C. S. Buer, G. O. Wasteneys, J. Masle, Ethylene modulates root-wave responses in *Arabidopsis*. *Plant Physiol.* **132**, 1085–1096 (2003).
40. R. L. Bishop, There is more than one way to frame a curve. *Am. Math. Mon.* **82**, 246–251 (1975).
41. R. Bastien, T. Bohr, B. Moulia, S. Douady, Unifying model of shoot gravitropism reveals proprioception as a central feature of posture control in plants. *Proc. Natl. Acad. Sci. U.S.A.* **110**, 755–760 (2013).
42. R. Bastien, Y. Meroz, The kinematics of plant nutation reveals a simple relation between curvature and the orientation of differential growth. *PLoS Comput. Biol.* **12**, e1005238 (2016).
43. J. Roué *et al*., Root cap size and shape influence responses to the physical strength of the growth medium in *Arabidopsis thaliana* primary roots. *J. Exp. Bot.* **71**, 126–137 (2019).
44. M. Quiros, M. B. Bogeat-Triboulot, E. Couturier, E. Kolb, Plant root growth against a mechanical obstacle: the early growth response of a maize root facing an axial resistance is consistent with the Lockhart model. *J. R. Soc. Interface* **19**, 20220266 (2022).
45. E. B. Blancaflor, J. M. Fasano, S. Gilroy, Mapping the functional roles of cap cells in the response of *Arabidopsis* primary roots to gravity. *Plant Physiol.* **116**, 213–222 (1998).
46. Z. Zhang, D. van Ophem, R. Chelakkot, N. Lazarovitch, I. Regev, A mechano-sensing mechanism for waving in plant roots. *Sci. Rep.* **12**, 1–12 (2022).
47. T. Baumberger, C. Caroli, O. Ronsin, Self-healing slip pulses along a gel/glass interface. *Phys. Rev. Lett.* **88**, 075509 (2002).
48. K. Shinomiya, H. Mayama, Y. Nonomura, Anomalous friction between agar gels under accelerated motion. *Langmuir* **34**, 12723–12729 (2018).
49. S. Thitamadee, K. Tuchihara, T. Hashimoto, Microtubule basis for left-handed helical growth in *Arabidopsis*. *Nature* **417**, 193–196 (2002).
50. M. Nakamura, T. Hashimoto, Mechanistic insights into plant chiral growth. *Symmetry* **12**, 2056 (2020).

51. I. Furutani *et al*., The spiral genes are required for directional control of cell elongation in *Arabidopsis thaliana*. *Development* **127**, 4443–4453 (2000).
52. B. Qi, H. Zheng, Modulation of root-skewing responses by KNAT 1 in *Arabidopsis thaliana*. *Plant J.* **76**, 380–392 (2013).
53. S. M. Swarbreck, Y. Guerringue, E. Matthus, F. J. Jamieson, J. M. Davies, Impairment in karrikin but not strigolactone sensing enhances root skewing in *Arabidopsis thaliana*. *Plant J.* **98**, 607–621 (2019).
54. A. Tekinalp et al., PyElastica. Zenodo. https://doi.org/10.5281/zenodo.7931429. Deposited 12 May 2023.
55. A. Tekinalp *et al.*, Topology, dynamics, and control of an octopus-analog muscular hydrostat. arXiv [Preprint] (2023). http://arxiv.org/abs/2304.08413.
56. X. Zhang, F. K. Chan, T. Parthasarathy, M. Gazzola, Modeling and simulation of complex dynamic musculoskeletal architectures. *Nat. Commun.* **10**, 1–12 (2019).
57. N. Naughton *et al*., Elastica: A compliant mechanics environment for soft robotic control. *IEEE Robot. Autom. Lett.* **6**, 3389–3396 (2021).
58. X. Zhang, N. Naughton, T. Parthasarathy, M. Gazzola, Friction modulation in limbless, three-dimensional gaits and heterogeneous terrains. *Nat. Commun.* **12**, 1–8 (2021).
59. N. Weiner, Y. Bhosale, M. Gazzola, H. King, Mechanics of randomly packed filaments–the "bird nest" as meta-material. *J. Appl. Phys.* **127**, 050902 (2020).
60. Y. Bhosale *et al*., Micromechanical origin of plasticity and hysteresis in nestlike packings. *Phys. Rev. Lett.* **128**, 198003 (2022).
61. N. Charles, M. Gazzola, L. Mahadevan, Topology, geometry, and mechanics of strongly stretched and twisted filaments: Solenoids, plectonemes, and artificial muscle fibers. *Phys. Rev. Lett.* **123**, 208003 (2019).
62. R. D. Kamien, The geometry of soft materials: A primer. *Rev. Mod. Phys.* **74**, 953 (2002).
63. C. S. Buer, J. Masle, G. O. Wasteneys, Growth conditions modulate root-wave phenotypes in *Arabidopsis*. *Plant Cell Physiol.* **41**, 1164–1170 (2000).
64. A. Porat, M. Rivière, Y. Meroz, A quantitative model for spatio-temporal dynamics of root gravitropism. *J. Exp. Bot.* **75**, erad383 (2023).
65. M. Wooten, I. Walker, "A novel vine-like robot for in-orbit inspection" in *Proceedings 45th International Conference on Environmental Systems* (Bellevue, WA, 2015), pp. 1–11.
66. L. H. Blumenschein, A. M. Okamura, E. W. Hawkes, Modeling of bioinspired apical extension in a soft robot. *Living Mach.* (2016).
67. A. Sadeghi, A. Mondini, B. Mazzolai, Toward self-growing soft robots inspired by plant roots and based on additive manufacturing technologies. *Soft Robot.* 211–223 (2017).
68. E. W. Hawkes, L. H. Blumenschein, J. D. Greer, A. M. Okamura, A soft robot that navigates its environment through growth. *Sci. Robot.* **2**, eaan3028 (2017).
69. F. Bizet, A. G. Bengough, I. Hummel, M. B. Bogeat-Triboulot, L. X. Dupuy, 3D deformation field in growing plant roots reveals both mechanical and biological responses to axial mechanical forces. *J. Exp. Bot.* **67**, 5605–5614 (2016).